Journal of Computational Physics 229 (2010) 921–932

Contents lists available at ScienceDirect

Journal of Computational Physics

journal homepage: www.elsevier.com/locate/jcp

Domain compression via anisotropic metamaterials designed by coordinate transformations

Ozlem Ozgun [a,*], Mustafa Kuzuoglu [b]

[a] Department of Electrical Engineering, Middle East Technical University, Northern Cyprus Campus, Guzelyurt, via Mersin 10, Turkey
[b] Department of Electrical Engineering, Middle East Technical University, 06531 Ankara, Turkey

ARTICLE INFO

Article history:
Received 5 March 2009
Received in revised form 9 October 2009
Accepted 12 October 2009
Available online 17 October 2009

Keywords:
Domain compression
Anisotropic metamaterials
Coordinate transformation
Finite element method
Cloaking

ABSTRACT

We introduce a spatial coordinate transformation technique to compress the excessive white space (i.e. free-space) in the computational domain of finite methods. This approach is based on the form-invariance property of Maxwell's equations under coordinate transformations. Clearly, Maxwell's equations are still satisfied inside the transformed space, but the medium turns into an anisotropic medium whose constitutive parameters are determined by the coordinate transformation. The proposed technique can be employed to reduce the number of unknowns especially in high-frequency applications wherein a finite method requires an electrically-large computational domain. After developing the analytical background of this technique, we report some numerical results for finite element simulations of electromagnetic scattering problems.

1. Introduction

Form-invariance property of Maxwell's equations under any coordinate transformation has led to numerous interesting and useful applications, which control the propagation of electromagnetic fields in a desired manner. Inside the transform space, Maxwell's equations are still satisfied, but the medium turns into an anisotropic medium, whose constitutive parameters are determined by the coordinate transformation, to reflect the effect of the coordinate transformation on the electromagnetic fields. One of the most well-known applications utilizing the coordinate transformation technique is the design of perfectly matched layers (PMLs), which are used as artificial absorbers in mesh truncation of the finite methods [1,2]. Another application, which is quite familiar to the physics community, is the design of a cloaking device for obtaining electromagnetic invisibility [3]. Recently, various anisotropic metamaterial (AMM) design techniques that are based on the concept of coordinate transformation have been proposed, some of which are listed in [4–14].

In this paper, we define a special coordinate transformation technique to compress the excessive white space, which is inevitable in some boundary value problems, in such a way that electromagnetic waves are bended and guided inside the AMM layer(s) without altering the wave behavior in the remaining part of the domain. To visualize a possible wave behavior inside the AMM layer (see Fig. 1), we may employ the ray-optics interpretation in high frequencies and show the confinement of the wave into the layer, which is designed above a thin perfect electric conductor (PEC) strip, assuming that the domain is compressed vertically. This figure is just an illustration to better grasp the action of an AMM layer, and the actual wave behavior may vary depending on how the compression operation is performed. It is worth to emphasize that the

* Corresponding author. Address: Department of Electrical Engineering, Middle East Technical University, Northern Cyprus Campus, Guzelyurt via Mersin 10, Turkey. Tel.: +90 392 661 2972.
E-mail addresses: ozozgun@metu.edu.tr, ozgunozlem@gmail.com (O. Ozgun).
URL: http://www.metu.edu.tr/~ozozgun (O. Ozgun).

0021-9991/$ - see front matter © 2009 Elsevier Inc. All rights reserved.
doi:10.1016/j.jcp.2009.10.023

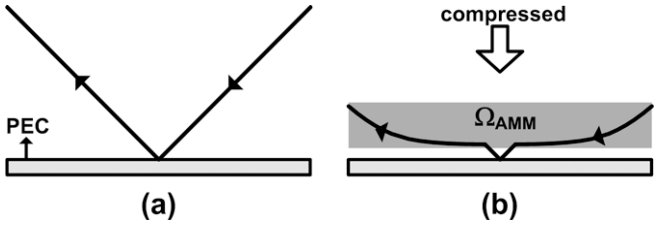

Fig. 1. Illustration of wave behavior inside the AMM layer: (a) original wave behavior and (b) guided and bended wave behavior after domain compression.

proposed method is applicable over the entire spectrum, not only in the high-frequency regime, because the derivations in this method follow exactly from Maxwell's equations.

The domain compression technique can be used to achieve efficient and accurate numerical simulations of electromagnetic boundary value problems by finite methods in the solution of a certain class of problems, especially having an electrically-large non-convex object or multiple objects positioned arbitrarily in space. In such problems, the computational domain requires the employment of *excessive* white-space (i.e. free-space), which introduces a large number of unknowns. This is due to the fact that the computational domain must necessarily be convex in order to properly take into account of the wave interactions (or mutual couplings) between different portions of the object(s). For instance, while solving the two-dimensional (2D) scattering problem containing an arbitrary non-convex object, the computational domain should be rectangular as shown in Fig. 2(a) (this is a commonly-used approach in literature for methods employing a Cartesian mesh/grid), or at least must be designed by considering the convex hull [i.e., the smallest convex set that encloses the object(s)] as shown in Fig. 2(b). The rays in Fig. 2(a) illustrate possible paths of wave interactions (reflected or diffracted waves), when the principles of ray optics are employed assuming that the object is electrically-large. It is evident that, in both cases in Fig. 2, the computational domain must include the excessive free-space covering the inner part of the convex hull of the object. Another reason of why the computational domain must be convex is that the PML (or any absorbing boundary condition), which truncates the computational domain, must be designed over a convex domain in order to annihilate outgoing waves arriving at the PML–free-space interface. Thus, the convexity property of the computational domain is mandatory in finite methods and introduces a large number of unknowns wasted in free-space in some challenging geometries. The proposed technique compresses excessive white space using AMM layer(s), as illustrated in Fig. 3, and thus, eliminates the unknowns in this white space and yields a reduction in the number of unknowns.

This paper is organized as follows: in Section 2, we introduce the fundamentals of the domain compression technique. In Section 3, we discuss some issues related to the implementation of the method. In Section 4, we present finite element simulations of a number of representative electromagnetic scattering problems. Finally, we present our conclusions in Section 5.

2. Domain compression by coordinate transformation

Without loss of generality, we illustrate the technique by considering the geometry in Fig. 4 where a two-dimensional L-shaped object is illuminated by a plane-wave. Let us assume that the original computational domain $\Omega_{c,\,org}$ is constructed as the spatial region containing the convex-hull of the object. That is, the original computational domain (i.e., $\Omega_{c,org} = \Omega_{FS} \cup \Omega_{PML} \cup \widetilde{\Omega}_{FS} \cup \widetilde{\Omega}_{PML} \cup \Omega_{AMM}$, where the subscripts 'FS' and 'PML' are the abbreviations for 'free-space' and 'perfectly matched layer', respectively) is trapezoidal in shape in order to minimize the number of unknowns as much as possible. The computational domain may also have a rectangular shape to be able to employ certain numerical schemes based on Cartesian grids. The initial phase of the procedure is the construction of the spatial region occupied by the AMM layer (Ω_{AMM}) in such a way that the excessive white space region is compressed suitably. The new computational domain now

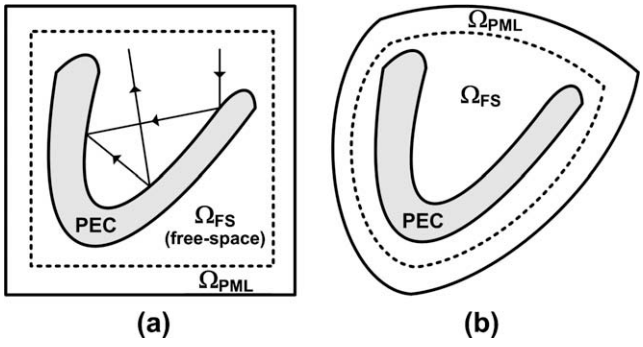

Fig. 2. Computational domain for non-convex object: (a) conventional rectangular domain and (b) domain with respect to the convex hull.

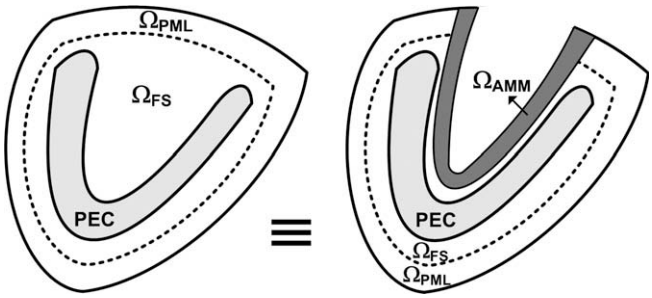

Fig. 3. Illustration of domain compression via AMM layer.

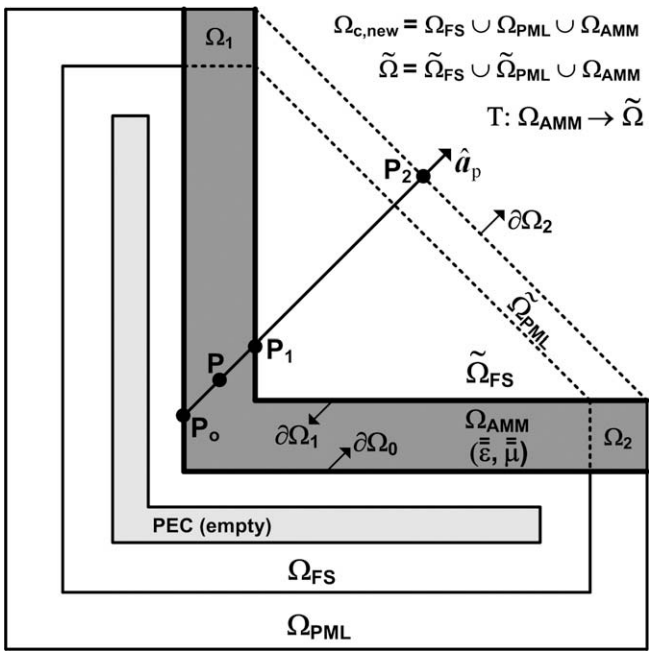

Fig. 4. Design of the AMM layer with coordinate transformation.

becomes $\Omega_{c,\,new} = \Omega_{FS} \cup \Omega_{PML} \cup \Omega_{AMM}$ as shown in Fig. 4. In this configuration, there may be a small free-space gap between the object and the boundary of the AMM layer ($\partial\Omega_0$).

To design the AMM layer, each point P inside the AMM layer is mapped to $\widetilde{P}$ inside the transformed region $\widetilde{\Omega} = \widetilde{\Omega}_{FS} \cup \widetilde{\Omega}_{PML} \cup \Omega_{AMM}$. This mapping is defined as a coordinate transformation $T : \Omega_{AMM} \to \widetilde{\Omega}$ as follows:

$$\widetilde{\vec{r}} = \frac{\|\vec{r}_2 - \vec{r}_0\|}{\|\vec{r}_1 - \vec{r}_0\|}(\vec{r} - \vec{r}_0) + \vec{r}_0 \tag{1}$$

where $\vec{r}$ and $\widetilde{\vec{r}}$ are the position vectors of the points P and $\widetilde{P}$ in the original and transformed coordinate systems, respectively, and $\|\cdot\|$ represents the Euclidean norm. Moreover, $\vec{r}_0$, $\vec{r}_1$ and $\vec{r}_2$ are the position vectors of P_0, P_1 and P_2 which are determined on $\partial\Omega_0$, $\partial\Omega_1$ and $\partial\Omega_2$, respectively, through the unit vector $\hat{a}_p$. The coordinate transformation $T : \Omega_{AMM} \to \widetilde{\Omega}$ maps the region Ω_{AMM} into the convex region $\widetilde{\Omega}$. In other words, the problem in Fig. 4 is solved as if the region $\widetilde{\Omega}$ is compressed into the AMM layer Ω_{AMM} in the direction of the unit vector $\hat{a}_p$. The direction of the unit vector $\hat{a}_p$ can be chosen in various ways (such as in the direction of parallel lines), and we will discuss the implementation issues in detail in Section 3.

As a result of the coordinate transformation in (1), the original medium turns into a spatially-varying anisotropic medium ensuring that the original forms of Maxwell's equations are still preserved in the transformed space. In other words, Maxwell's equations are form-invariant under space transformations, and a general coordinate transformation leads to the following expressions for the permittivity and permeability tensors [15,16]

$$\bar{\bar{\varepsilon}} = \varepsilon\overline{\overline{\Lambda}} \tag{2a}$$

$$\bar{\bar{\mu}} = \mu\overline{\overline{\Lambda}} \tag{2b}$$

where ε and μ are the constitutive parameters of the original isotropic medium (usually free-space in scattering problems), and

$$\overline{\overline{\Lambda}} = \left(\bar{\bar{J}}^{-1}\right)^{T} \cdot \left(\bar{\bar{J}}^{-1}\right) \Big/ \det\left(\bar{\bar{J}}^{-1}\right) \tag{3}$$

where $\bar{\bar{J}}$ is the Jacobian tensor defined as (in Cartesian coordinates)

$$\bar{\bar{J}} = \frac{\partial(\tilde{x},\tilde{y},\tilde{z})}{\partial(x,y,z)} = \begin{bmatrix} \partial\tilde{x}/\partial x & \partial\tilde{x}/\partial y & \partial\tilde{x}/\partial z \\ \partial\tilde{y}/\partial x & \partial\tilde{y}/\partial y & \partial\tilde{y}/\partial z \\ \partial\tilde{z}/\partial x & \partial\tilde{z}/\partial y & \partial\tilde{z}/\partial z \end{bmatrix}. \tag{4}$$

Hence, the AMM layer can be designed using the constitutive parameters in (2), which are directly computed by using the Jacobian of the transformation.

The coordinate transformation in (1) yields real-valued coordinates in the transformed space. However, if the transformed point $\tilde{\vec{r}}$ falls into the PML region of the original domain (i.e., $\tilde{\vec{r}} \in \widetilde{\Omega}_{\text{PML}} \cup \Omega_1 \cup \Omega_2$ in Fig. 4), then the PML action should be included in order to achieve an attenuation in the field quantities in the close vicinity of $\partial\Omega_1$. In other words, the PML region should also be compressed into a region inside the AMM layer. This is necessary in order to avoid the artificial reflections from the outer boundary $\partial\Omega_1$. Inclusion of the PML action can be handled via two alternative ways depending on the implementation of the PML. First, the PML can be realized as an anisotropic layer with suitably defined permittivity and permeability tensors ($\bar{\bar{\varepsilon}}_{\text{PML}}$, $\bar{\bar{\mu}}_{\text{PML}}$). If the constitutive parameters of the PML region in the original domain are calculated using a suitable PML approach, then the constitutive parameters of the AMM layer whose transformed points are inside the PML region should be determined as follows:

$$\bar{\bar{\varepsilon}} = \varepsilon\left(\bar{\bar{J}}^{-1}\right)^{T} \cdot \bar{\bar{\varepsilon}}_{\text{PML}} \cdot \left(\bar{\bar{J}}^{-1}\right) \Big/ \det\left(\bar{\bar{J}}^{-1}\right) \tag{5a}$$

$$\bar{\bar{\mu}} = \mu\left(\bar{\bar{J}}^{-1}\right)^{T} \cdot \bar{\bar{\mu}}_{\text{PML}} \cdot \left(\bar{\bar{J}}^{-1}\right) \Big/ \det\left(\bar{\bar{J}}^{-1}\right). \tag{5b}$$

Second, as an alternative and more convenient way, the PML action can be included using the locally-conformal PML method [2], which utilizes a special type of complex coordinate stretching. The locally-conformal PML is designed in complex space by just replacing the real coordinates with their complex counterparts (i.e., simply by adding suitable imaginary parts to the real coordinates), which are calculated in terms of the complex coordinate transformation. Thus, the transformed points ($\tilde{\vec{r}} \in \Re^3$) falling into the PML region are replaced by their complex counterparts calculated by the following complex coordinate transformation

$$\tilde{\vec{r}} \to \tilde{\vec{r}}_c = \tilde{\vec{r}} + \frac{\alpha \xi^m}{jkm\, d_{\text{PML}}^{m-1}} \hat{a}_\xi, \tag{6}$$

where $\tilde{\vec{r}}_c \in C^3$, ξ is the distance between $\tilde{\vec{r}}$ and $\vec{r}_0$ ($\vec{r}_0$ is the point on the PML–free-space interface which is closest to $\tilde{\vec{r}}$), $\hat{a}_\xi$ is the unit vector along the direction of decay (i.e., in the direction $\tilde{\vec{r}} - \vec{r}_0$), k is the wavenumber, α is a positive parameter, m is a positive integer, and d_{PML} is the local PML thickness for the corresponding PML point. After the transformations in (1) and (6) are performed sequentially, the constitutive parameters of the AMM layer should be similarly calculated using the expressions in (2), (3), (4), for the point $\tilde{\vec{r}}_c$. It is useful to note that the constitutive parameters in this case become complex-valued reflecting the effect of the PML action.

3. Implementation issues

While performing the coordinate transformation in (1), the selection of the unit vector $\hat{a}_p$ (see Fig. 4) plays a vital role in determining how the domain will be compressed, or clearly in which direction the domain will be squeezed into the spatial region occupied by the AMM layer. There may be various ways to achieve this goal, but some rules of thumb should be kept in mind to properly compress the domain. First, the coordinate transformation $T : \Omega_{\text{AMM}} \to \widetilde{\Omega}$ in (1) must be continuous such that:

$$\|T(\vec{r}) - T(\vec{r}^*)\| < \varepsilon, \quad \text{whenever } \|\vec{r} - \vec{r}^*\| < \delta, \tag{7}$$

where $\varepsilon > 0$ and $\delta > 0$ (δ depends on ε). The expression in (7) implies that two closely-located points $\vec{r}$ and $\vec{r}^*$ in Ω_{AMM} are mapped to also closely-located points $\tilde{\vec{r}}$ and $\tilde{\vec{r}}^*$ in $\widetilde{\Omega}$. In other words, there should not be a considerable deviation in relative positions for two closely-located points after the coordinate transformation. Otherwise, unreliable results may occur due to two reasons: (i) spatial variations in the entries of the permittivity and permeability tensors corresponding to contiguous points increase owing to the definition of the coordinate transformation, and (ii) qualities of elements in the mesh are distorted to a great degree. This conclusion is critical in the simulation of the technique, as demonstrated in Section 4. In addition to this principal requirement, the unit vector $\hat{a}_p$ should be chosen in such a way that the domain should be compressed in a symmetrical way as much as possible, in conformity with the spatial symmetry of the computational domain. This may

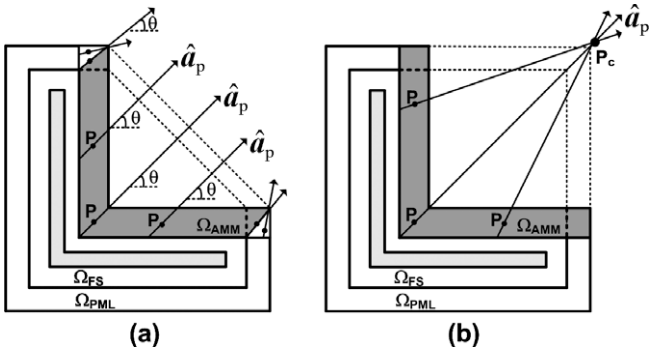

Fig. 5. Implementation of coordinate transformation: (a) unit vector chosen in the direction of parallel lines and (b) unit vector chosen in the direction of a center.

be important in order to avoid non-uniform compression (i.e., non-uniform density of transformed points) inside the AMM layer, and thus, to avoid large variances in the entries of the constitutive tensors.

Depending on the geometry of the problem, the unit vector $\hat{a}_p$ can be chosen in the direction of parallel lines and/or in the direction of lines intersecting at a given center point. For instance, for the L-shaped object shown in Fig. 5(a), the unit vector $\hat{a}_p$ can be directed along the parallel lines making an angle θ which corresponds to the angle of the line passing through the corners of the object. Then, the points P_0, P_1 and P_2 are determined on their corresponding boundaries through $\hat{a}_p$. In Fig. 5(a), in the whitened triangular sections of the AMM layer inside the PML region, the unit vector $\hat{a}_p$ is directed with different angles as shown in the figure. In fact, in these small portions, the transformed coordinates are identical to the original coordinates (i.e., $\vec{\tilde{r}} = \vec{r}$ and Jacobian tensor in (4) is unity) because P_1 and P_2 coincide exactly at the tip of the boundary.

As an alternative way, the direction of the unit vector $\hat{a}_p$ can be chosen in the direction of lines intersecting at a pre-defined center point, which is slightly outside the compressed domain. This approach is inspired by the multi-center PML method introduced in [17]. For example, we now consider the L-shaped object in a rectangular computational domain (it may also be trapezoidal) as shown in Fig 5(b). In this case, we may choose the center point (P_c) to be located close to the upper right corner of the domain. Then, the unit vector $\hat{a}_p$ denotes the direction of the vector from each point P inside the AMM layer towards to the center P_c. These two alternative ways in the calculation of $\hat{a}_p$ may both yield reliable results. In general, we have observed that if the geometry of the AMM layer contains corners with wide angles (such as $\geqslant 90^\circ$), then the former approach considering parallel lines may be used easily to achieve the compression. On the other hand, in the case of narrower angles, the second approach based on a center may be employed in a more convenient manner. In this case, the center which is located in the close neighborhood of the mid-point (or the vertex, if any) of the boundary $\partial\Omega_2$ is a good candidate to achieve desirable results.

At first sight, it may be claimed that the AMM layer requires finer grid to better handle the spatial variations, because a larger domain is compressed into a smaller domain. Here, we explain why we claim that the proposed approach reduces the number of unknowns, and that the anisotropic material does *not* necessarily have to be denser. First, we emphasize that the "electrically-large" objects are of interest to us due to the large number of unknowns needed in such high-frequency problems. If the size of the object is large with respect to the wavelength, we can use the principles of the ray-optics to describe the physics of the problem. Let us assume that the scatterer is an L-shaped object, and the incident plane wave illuminates the object at an arbitrary angle, as shown in Fig. 6(a). This figure shows the 1st- and 2nd-order reflected rays from the lower and upper faces, respectively, for the original problem. In Fig. 6(b), we show the equivalent problem where the domain is compressed in the direction of $\hat{a}_p$ unit vector, which is in the same direction of the incident field. The 1st- and 2nd-order reflected rays after the coordinate transformation are shown by $1'$ and $2'$, respectively. Obviously, the length of the 1st ray will *always* be longer than its original length $(\ell_{1'} > \ell_1)$ because of the compression, irrespective of the point where the incident wave hits the object. Hence, the ray must travel faster in order to traverse over this longer path. Since the frequency is fixed, the wavelength increases, and therefore, the spatial discretization (or element size) in the original problem is sufficient, even provides better resolution, in the equivalent problem to handle field variations over this longer path. Now, let us examine the 2nd-order reflected ray $2'$. It is evident that the length of the $2'$ ray gets shorter after the transformation, and a finer discretization is required over this path due to shorter wavelength. Therefore, the only source of error will be the rough discretization over $2'$ if the element size of the original problem is employed. However, since the effect (and the strength) of the 2nd-order ray is obviously less than of the 1st-order ray, the error contribution remains in acceptable levels (as demonstrated in numerical simulations). More importantly, it is possible to decrease the error by increasing the length of the $2'$ ray. The worst case for which the length of the $2'$ ray is the shortest occurs if the direction of $2'$ is in the same direction as the $-\hat{a}_p$ unit vector (direction of compression), as shown in Fig. 6(b). If we change the direction of $-\hat{a}_p$ unit vector as shown in Fig. 6(c), then the length of the 2nd-order ray increases $(\ell_{2''} > \ell_{2'})$, and the error due to discretization decreases. In principle, if there is wave propagation in the direction of compression, it introduces errors based on the compression rate because of the decrease in the length of propagation. Otherwise, the discretization error will not occur. Hence, by adjusting

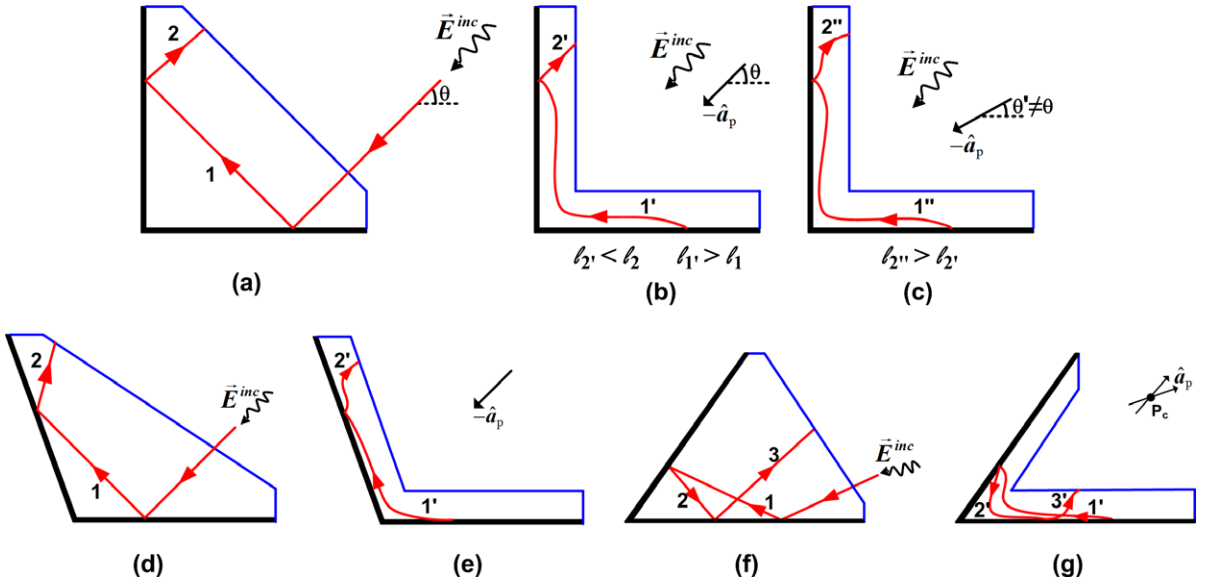

Fig. 6. Ray-optics interpretation of domain compression technique for electrically-large objects: (a) rays in original problem of L-shaped object, (b) rays in AMM layer if the directions of compression and propagation are the same, (c) rays in AMM layer if the directions of compression and propagation are different, (d) rays in original problem of wide-angle object, (e) rays in AMM layer of wide-angle object, (f) rays in original problem of narrow-angle object and (g) rays in AMM layer of narrow-angle object.

the direction of compression based on the physics of the problem at hand, we can achieve reliable results and decrease the number of unknowns without using finer meshes. We note that since we compress the region between different parts of a non-convex object, the waves propagating in the direction of compression will usually be the 2nd- or higher-order waves, whose error contribution due to discretization will be small. For the purpose of illustration, we show the ray propagation inside a wide-angle object in Fig. 6(d) and (e), and inside a narrow-angle object in Fig. 6(f) and (g). In Fig. 6(e), the only source of error is the 2nd-order ray, however, we will never experience the worst-case where the compression direction is in the direction of propagation due to the geometry and the direction of $\hat{a}_p$. Similarly, in Fig. 6(g), only the 3rd-order ray will cause error because of the same principles. It is also worthwhile to mention that we do not consider the incident ray in Fig. 6(b), (c), (e) and (g), because we use the scattered field formulation, where $E_z^{scat} = -E_z^{inc}$ is imposed on the boundary of the conducting object. Clearly, we are interested in only the scattered fields. The above-mentioned comments are applicable to the diffracted fields as well. The length of the 1st-order diffracted field originated from an edge always increases after the transformation, implying that the discretization of the original problem is adequate for reliable results.

It is useful to emphasize that the computational effort to implement the coordinate transformation in a computer code creates almost negligible burden on the processing power of the computer, compared to some other phases of the code (such as usual matrix construction and solution phases), because the calculation of the constitutive parameters using the Jacobian of the coordinate transformation in (4) can be carried out in the preprocessing phase (i.e., before the matrix construction phase). The calculation of the Jacobian of the coordinate transformation can be performed analytically or numerically depending on the geometry and on the nature of the finite method utilized in the solution. In the simulation of the method in a finite element method (FEM) code, the Jacobian of the coordinate transformation can be calculated numerically using a very simple and straightforward procedure, even in challenging geometries. We briefly discuss this procedure in Section 3.1.

3.1. Numerical implementation in finite element method

In this section, we briefly present the numerical evaluation of the Jacobian of the coordinate transformation given in (4). The initial step, which is performed in the preprocessing phase, is to compute the transformed coordinates for all nodes inside the AMM layer by using (1). In this equation, the position vectors that are located on their corresponding boundaries can be found from the node coordinates in an existing FEM mesh by using some simple computational search techniques, assuming that the nodes on the boundaries of the AMM layer (i.e., $\partial\Omega_0$, $\partial\Omega_1$) are preserved during the mesh generation phase. We should also have information about the boundary $\partial\Omega_2$ either analytically or numerically.

After applying the coordinate transformation to all nodes inside the AMM layer, the Jacobian tensor in (4) is calculated using the scalar FEM shape functions (i.e., basis functions) in each element of the AMM layer. Thus, this numerical calculation can be incorporated into the matrix construction phase with little effort. We first assume that the computational domain is discretized by tetrahedral elements in 3D. Then, in each element, we express the coordinate variable variations in terms of

the scalar shape functions and the global node coordinates (in Cartesian coordinates) using the *isoparametric mapping*[1] as follows

$$x = \sum_{i=1}^{4} x_i N_i(\varepsilon,\eta,\upsilon), \quad y = \sum_{i=1}^{4} y_i N_i(\varepsilon,\eta,\upsilon), \quad z = \sum_{i=1}^{4} z_i N_i(\varepsilon,\eta,\upsilon), \tag{8}$$

where (x_i, y_i, z_i) are the node coordinates in each tetrahedral element, and $N_i(\varepsilon,\eta,\upsilon)$ is the scalar shape function for the ith node in local coordinates and given by

$$N_1 = 1-\varepsilon-\eta-\upsilon, \quad N_2 = \varepsilon, \quad N_3 = \eta, \quad N_4 = \upsilon. \tag{9}$$

Similarly, we express the variations in the transformed coordinates as follows:

$$\tilde{x} = \sum_{i=1}^{4} \tilde{x}_i N_i(\varepsilon,\eta,\upsilon), \quad \tilde{y} = \sum_{i=1}^{4} \tilde{y}_i N_i(\varepsilon,\eta,\upsilon), \quad \tilde{z} = \sum_{i=1}^{4} \tilde{z}_i N_i(\varepsilon,\eta,\upsilon) \tag{10}$$

where $(\tilde{x}_i, \tilde{y}_i, \tilde{z}_i)$ are the node coordinates after the coordinate transformation in (1). Then, using the *chain rule*, we derive the following expressions for the components of the Jacobian tensor in (4) after some manipulations

$$\begin{bmatrix} \partial\tilde{x}/\partial x \\ \partial\tilde{x}/\partial y \\ \partial\tilde{x}/\partial z \end{bmatrix} = J_{\text{FEM}} \cdot \begin{bmatrix} \partial\tilde{x}/\partial\varepsilon \\ \partial\tilde{x}/\partial\eta \\ \partial\tilde{x}/\partial\upsilon \end{bmatrix} \tag{11a}$$

$$\begin{bmatrix} \partial\tilde{y}/\partial x \\ \partial\tilde{y}/\partial y \\ \partial\tilde{y}/\partial z \end{bmatrix} = J_{\text{FEM}} \cdot \begin{bmatrix} \partial\tilde{y}/\partial\varepsilon \\ \partial\tilde{y}/\partial\eta \\ \partial\tilde{y}/\partial\upsilon \end{bmatrix} \tag{11b}$$

$$\begin{bmatrix} \partial\tilde{z}/\partial x \\ \partial\tilde{z}/\partial y \\ \partial\tilde{z}/\partial z \end{bmatrix} = J_{\text{FEM}} \cdot \begin{bmatrix} \partial\tilde{z}/\partial\varepsilon \\ \partial\tilde{z}/\partial\eta \\ \partial\tilde{z}/\partial\upsilon \end{bmatrix} \tag{11c}$$

where

$$J_{\text{FEM}} = \begin{bmatrix} \partial x/\partial\varepsilon & \partial y/\partial\varepsilon & \partial z/\partial\varepsilon \\ \partial x/\partial\eta & \partial y/\partial\eta & \partial z/\partial\eta \\ \partial x/\partial\upsilon & \partial y/\partial\upsilon & \partial z/\partial\upsilon \end{bmatrix}^{-1} \tag{12}$$

All derivative terms appearing on the right-hand-side of the equations in (11) and (12), which are also the entries of the Jacobian tensor in (4), can be calculated simply by using the expressions in (8)–(10), and depend directly on the nodal coordinates. Next, the constitutive tensors in each element can be calculated using (2) and (3) with some simple matrix algebra. If the PML action is to be included into the transformation, the transformed coordinates $\vec{\tilde{r}}$ in (11) and (10) are just replaced by the complex coordinates $\vec{\tilde{r}}_c$ calculated by (6). A similar approach is followed for 2D problems involving triangular elements. In this case, we omit the z- and υ-variation in global and local coordinates, respectively. We also set the number of nodes to three instead of four in the summation terms in (8) and (10). We emphasize that the Jacobian, as well as the constitutive parameters, are evaluated only in terms of the nodal coordinates. Hence, it is interesting that we can just replace the original coordinates with the transformed coordinates to implement the domain compression without computing the material parameters, and further decrease the computation time.

4. Finite element simulations

In this section, we present the results of a number of numerical experiments to validate the performance of the AMM layer in 2D TM_z electromagnetic scattering problems involving infinitely-long cylindrical PEC objects. All simulations are performed by using our FEM software employing triangular elements. In all examples, the wavelength in free-space (λ_0) is set to 1 m. In addition, the computational domain is terminated with a PML absorber, which is implemented by the locally-conformal PML method [2]. Moreover, in all examples involving a single object, the free-space distance between the object and the boundary of the AMM layer is set to $0.05\lambda_0$. In other examples involving multiple objects, this distance is shown clearly in their corresponding plots. The incident plane wave is assumed to be in the form of $\vec{E}^{inc} = \hat{a}_z \exp[jk(x\cos\varphi^{inc} + y\sin\varphi^{inc})]$, where φ^{inc} is the angle of incidence with respect to the x-axis.

In each example in this section, we simulate two scenarios:

[1] In isoparametric mapping, each element in global coordinates is mapped to a master element in local coordinates. In this mapping, both the global coordinates and the unknown field are expressed in terms of the same shape functions.

Table 1
Error values and reduction in unknowns for L-shaped scatterer (L, edge length of the scatterer; d_{AMM}, width of the AMM layer; Δh, element size in FEM).

L (m)	$d_{AMM}(m)$	*ERR* (%) (trapezoidal domain)		N_{reduce} (%)	
		$\Delta h = \lambda_0/20$	$\Delta h = \lambda_0/40$	Trapezoidal domain	Square domain
2	0.25	0.0473	0.0279	35	52
	0.2	0.0567	0.0462	37	54
	0.15	0.0851	0.0639	40	57
4	0.5	0.0336	0.0332	44	61
	0.3	0.0717	0.0666	51	68
	0.2	0.1057	0.1015	55	71
8	0.5	0.0713	0.0306	62	77
	0.4	0.0988	0.0942	65	80
	0.3	0.1700	0.1310	68	82

(i) simulation of the original problem, and
(ii) simulation of the equivalent problem compressed with AMM layer.

We expect that these simulations must yield identical field values inside the free-space region of scenario (ii) as shown in Fig. 4 (excluding the compressed domain in scenario (i)). Therefore, in order to measure the performance of the proposed method, we introduce a mean-square error criterion as follows

$$ERR = \frac{\sum_{\Omega_{FS}} \left| \vec{E}^{(ii)} - \vec{E}^{(i)} \right|^2}{\sum_{\Omega_{FS}} \left| \vec{E}^{(i)} \right|^2} \qquad (\%) \tag{13}$$

where $\vec{E}^{(i)}$ and $\vec{E}^{(ii)}$ are the electric fields calculated in the scenarios (i) and (ii), respectively, and Ω_{FS} is the above-mentioned free-space region in scenario (ii). It may be useful to mention that we perform scenario (i) only for the sake of comparison, and scenario (ii) does *not* require any information about the full-mesh of the original domain in scenario (i), but just need *a priori* knowledge about the geometry of the outer boundary $\partial\Omega_2$ and the PML boundary (viz., dotted boundaries in Fig. 4). The performance of the compression technique is also tested in terms of the radar cross section (RCS) calculations.

Apart from these performance evaluations, we measure the value of the reduction in the number of unknowns by using the following expression

$$N_{reduce} = \frac{N^{(i)} - N^{(ii)}}{N^{(i)}} \qquad (\%) \tag{14}$$

where $N^{(i)}$ and $N^{(ii)}$ are the number of unknowns employed in the scenarios (i) and (ii), respectively.

In the first example, we consider a scattering problem, where a plane wave ($\varphi^{inc} = 45^\circ$) is incident to an infinitely-long PEC cylinder having a 'thin' L-shaped cross-section whose thickness is $\lambda_0/20$. The element size is set to $\lambda_0/20$ for the original problem. We implement the coordinate transformation in scenario (ii) by using unit vectors directed along parallel lines with angle 45° (refer to the discussion in Section 3), which is indeed the worst case mentioned in Fig. 6(b). In Table 1, we tabulate the *ERR* values by varying the edge length of the object (L), the thickness of the AMM layer (d_{AMM}), and the element size (Δh) used in FEM, assuming that the computational domain is designed by considering the convex hull of the object (i.e., trapezoidal). We also tabulate the N_{reduce} values corresponding to the trapezoidal domain, as well as to the square domain. The results in this table reveal that the proposed method is reliable for arbitrarily-sized objects using electrically-thin AMM layers and using elements having moderate sizes. We observe that the results can obviously be improved by increasing the thickness of the layer, rather than decreasing the element size (refer to the discussion in Section 3). Due to the nature of the geometry, the method provides a considerable reduction in the number of unknowns, especially in high frequencies. To visualize the wave behavior in the computational domain, we consider an L-shaped object with edge length 8 m, and design an AMM layer whose thickness is 1 m. We plot the contours of the magnitude of the scattered electric field in Fig. 7(a) and (b) for the scenarios (i) and (ii), respectively. We also plot the bistatic RCS profiles in Fig. 7(c).

By referring to Fig. 6 described in Section 3, we plot the *ERR* values in Fig. 8 as a function of the direction of compression corresponding to an L-shaped object, whose edge length is 10 m, illuminated by an incident plane with $\varphi^{inc} = 45^\circ$. We note that the same mesh discretization $\lambda_0/20$ is employed uniformly for both original and equivalent problems. The black and red curves[2] correspond to the simulations where $d_{AMM} = 0.7$ m and $d_{AMM} = 1$ m, respectively. In the black curve, the maximum error occurs if the compression is performed in the same direction of propagation (i.e., 45°). However, when we change the compression direction, the error decreases because the length of the 2nd-order reflected ray (2′ in Fig. 6(c)) becomes longer.

[2] For interpretation of the references of color in this figure, the reader is referred to the web version of this article.

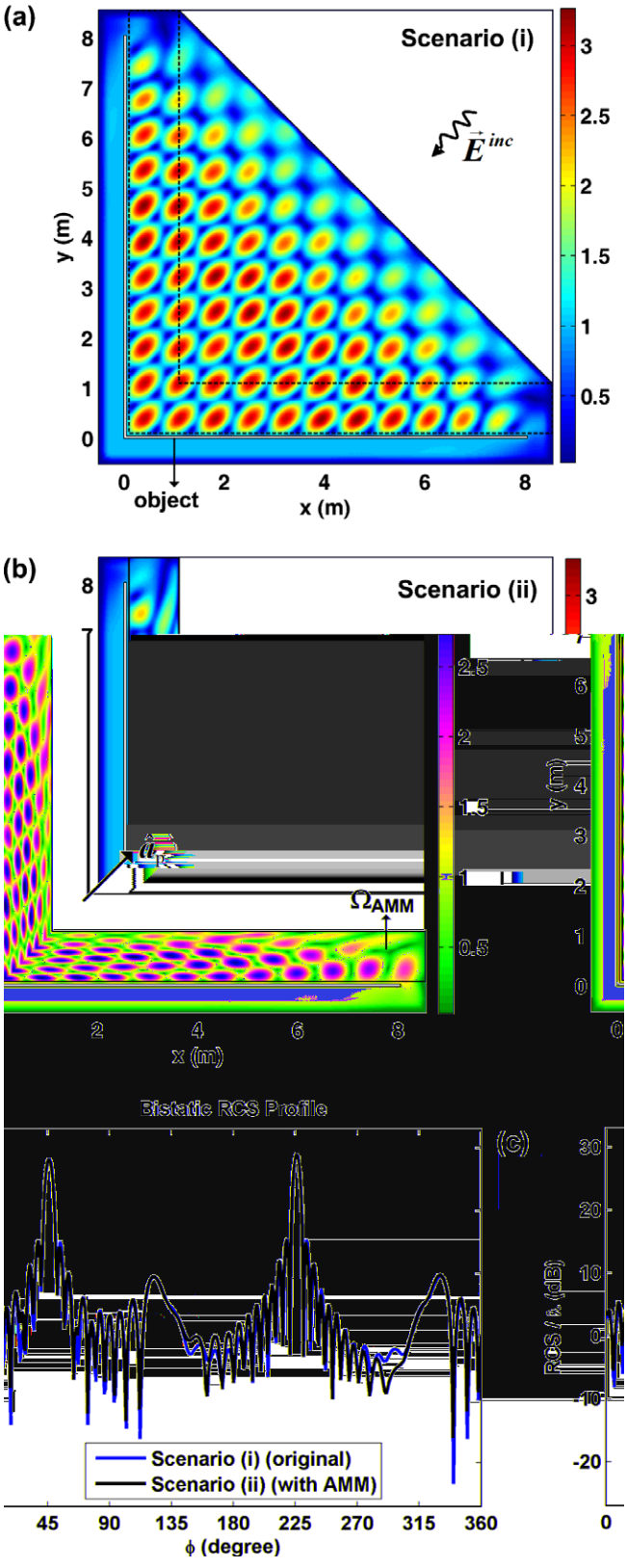

Fig. 7. Finite element simulation for L-shaped object: (a) electric field contour in original problem [scenario (i)], (b) electric field contour in equivalent problem with AMM layer [scenario (ii)] and (c) bistatic RCS profile.

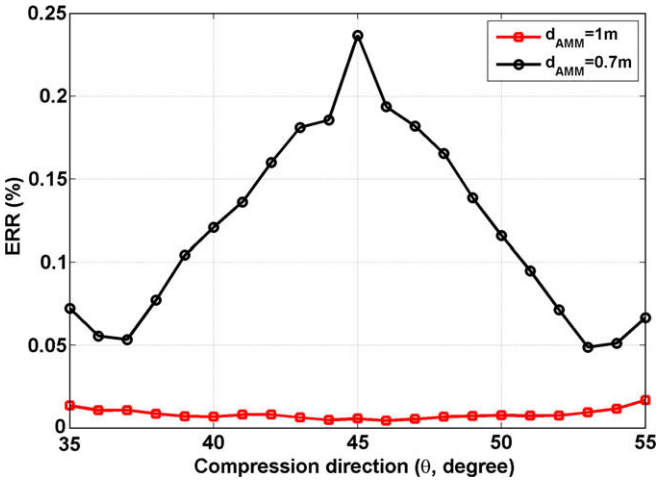

Fig. 8. Error values as a function of compression direction for L-shaped object.

For higher angles, the results start to deteriorate because of the increase in the elemental distortion caused by non-uniform compression. When we slightly change the thickness of the AMM layer ($d_{\mathrm{AMM}} = 1$ m), we observe that the error – shown by the red curve – considerably decreases even in the worst case, meaning that this thickness of the layer can easily handle the

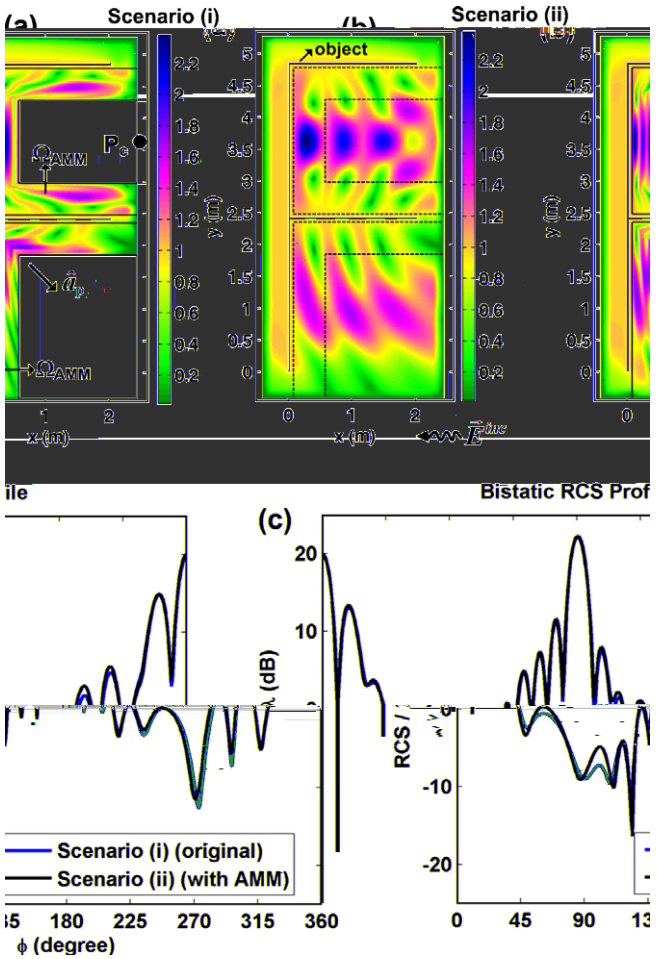

Fig. 9. Finite element simulation for F-shaped object: (a) electric field contour in original problem [scenario (i)], (b) electric field contour in equivalent problem with two AMM layers [scenario (ii)] and (c) bistatic RCS profile.

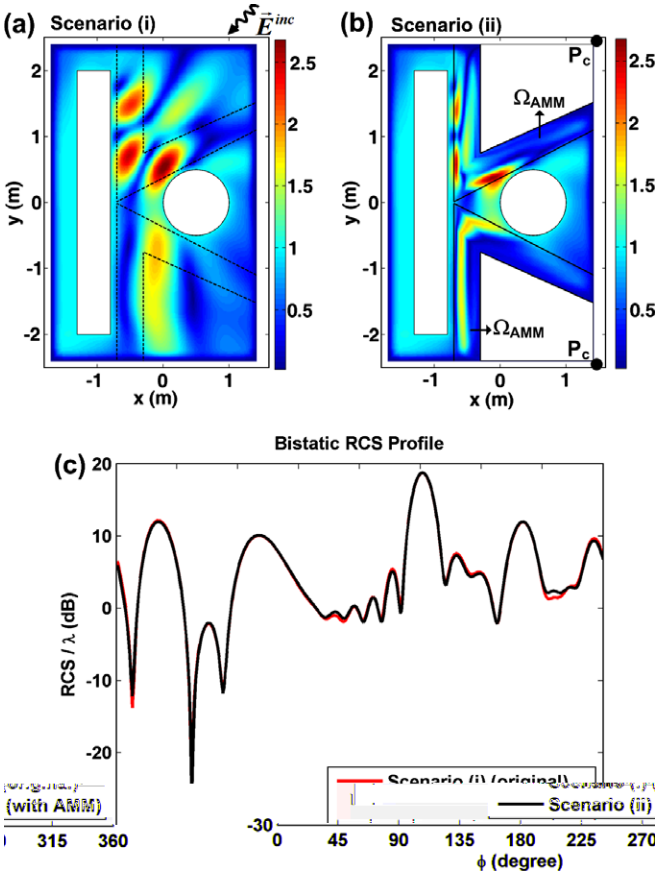

Fig. 10. Finite element simulation for multiple objects (a circular object in front of a rectangular object): (a) electric field contour in original problem [scenario (i)], (b) electric field contour in equivalent problem with two AMM layers [scenario (ii)] and (c) bistatic RCS profile.

Table 2
Computation time and number of unknowns in numerical experiments.

Description	Computation time (s)		Number of unknowns	
	Scenario (i)	Scenario (ii)	Scenario (i)	Scenario (ii)
L-shaped (8 m)	215.6	41.9	20,534	7843
F-shaped	110.7	69.7	14,784	8850
Two objects	77.6	47.7	11,814	7837

field variations without using finer grid. Therefore, we conclude that the results are in conformity with the discussions in Section 3, and the errors are in acceptable levels. Finally, as instrumental information, the reduction in unknowns is 60% if $d_{\mathrm{AMM}} = 0.7$ m, and 55% if $d_{\mathrm{AMM}} = 1$ m.

In the second example, we perform the domain compression for a thin F-shaped object illuminated by a plane wave with $\varphi^{inc} = 0^{\circ}$. We plot the scattered field contours and the bistatic RCS profiles in Fig. 9. In scenario (ii), we design two AMM layers whose widths are set to 0.5 m. The first AMM layer is designed inside the inlet-like structure (upper part) using unit vectors directed along the center ($\mathrm{P_c}$) shown by the black dot in Fig. 9(b). The second AMM layer is designed for the leg of the geometry (lower part) using unit vectors directed along parallel lines passing through the diagonal. The value of *ERR* is calculated as 0.5439%, and the reduction in unknowns as 40%.

The last example considers a scattering problem involving multiple objects. A plane wave ($\varphi^{inc} = 45^{\circ}$) illuminates a rectangular (0.5 m $\times$ 4 m) object and a circular object whose diameter is 1 m. We plot the scattered field contours and the bistatic RCS profiles in Fig. 10. As shown in Fig. 10(b), we design two AMM layers whose widths are set to 0.3 m using the centers ($\mathrm{P_c}$) shown by the black dots. We compute the *ERR* as 0.5448%, and the reduction in unknowns as 34%.

Finally, in order to manifest the decrease in the overall computation time, we tabulate the periods of time elapsed to process the examples in this section, as well as their number of unknowns, in Table 2. The simulations have been performed in an ordinary PC (Pentium 4 with 1 GB RAM) using MATLAB®.

The numerical experiments in this section demonstrate that the performance of the AMM layer in domain compression is in conformity with the theory, in various configurations.

5. Conclusions

In this paper, we have introduced a new technique employing anisotropic metamaterials for the purpose of domain compression in electromagnetic problems. The anisotropic metamaterial layer is implemented by a suitably-defined coordinate transformation. We have concluded that the proposed method provides a reduction in the number of unknowns, as well as in memory and computation time, which become more pronounced especially in high-frequency applications. We have numerically explored the functionality of the method in various configurations with the aid of finite element simulations, and have validated the theoretical predictions.

References

[1] W.C. Chew, W. Weedon, A 3D perfectly matched medium from modified Maxwell's equations with stretched coordinates, Microwave and Optical Technology Letters 7 (1994) 599–604.
[2] O. Ozgun, M. Kuzuoglu, Near-field performance analysis of locally-conformal perfectly matched absorbers via Monte Carlo simulations, Journal of Computational Physics 227 (2007) 1225–1245.
[3] J.B. Pendry, D. Schurig, D.R. Smith, Controlling electromagnetic fields, Science 312 (2006) 1780–1782.
[4] O. Ozgun, M. Kuzuoglu, Electromagnetic metamorphosis: reshaping scatterers via conformal anisotropic metamaterial coatings, Microwave and Optical Technology Letters 49 (2007) 2386–2392.
[5] O. Ozgun, M. Kuzuoglu, Utilization of anisotropic metamaterial layers in waveguide miniaturization and transitions, IEEE Microwave and Wireless Components Letters 17 (2007) 754–756.
[6] F. Kong, B.I. Wu, J.A. Kong, J. Huangfu, S. Xi, H. Chen, Planar focusing antenna design by using coordinate transformation technology, Applied Physics Letters 91 (2007) 253509.
[7] J. Huangfu, S. Xi, F. Kong, J. Zhang, H. Chen, D. Wang, B. Wu, L. Ran, J.A. Kong, Application of coordinate transformation in bent waveguides, Journal of Applied Physics 104 (2008) 014502.
[8] B. Donderici, F.L. Teixeria, Metamaterial blueprints for reflectionless waveguide bends, IEEE Microwave and Wireless Components Letters 18 (2008) 233–235.
[9] O. Ozgun, M. Kuzuoglu, Efficient finite element solution of low-frequency scattering problems via anisotropic metamaterial layers, Microwave and Optical Technology Letters 50 (2008) 639–646.
[10] Q. Wu, K. Zhang, F. Meng, L. Li, Material parameters characterization for arbitrary *N*-sided regular polygonal invisible cloak, Journal of Physics D: Applied Physics 42 (2009) 035408.
[11] B. Vasic, G. Isic, R. Gajic, K. Hingerl, Coordinate transformation based design of confined metamaterial structures, Physical Review B 79 (2009) 085103.
[12] D.-H. Kwon, D.H. Werner, Polarization splitter and polarization rotator designs based on transformation optics, Optics Express 16 (2008) 18731–18738.
[13] D.-H. Kwon, D.H. Werner, Transformation optical designs for wave collimators, flat lenses, and right-angle bends, New Journal of Physics 10 (2008) 115023.
[14] P.H. Tichit, S.N. Burokur, A. de Lustrac, Ultradirective antenna via transformation optics, Journal of Applied Physics 105 (2009) 104912.
[15] I.V. Lindell, Methods for Electromagnetic Field Analysis, Oxford University Press, 1992.
[16] G.W. Milton, M. Briane, J.R. Willis, On cloaking for elasticity and physical equations with a transformation invariant form, New Journal of Physics 248 (2006) 1–20.
[17] O. Ozgun, M. Kuzuoglu, Multi-center perfectly matched layer implementation for finite element mesh truncation, Microwave and Optical Technology Letters 49 (2007) 827–832.